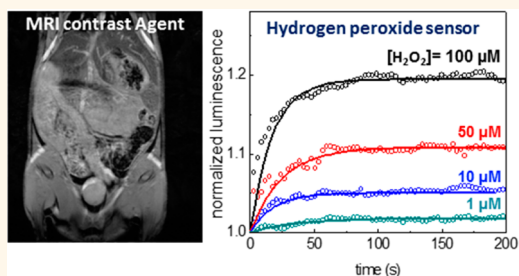


Multifunctional Rare-Earth Vanadate Nanoparticles: Luminescent Labels, Oxidant Sensors, and MRI Contrast Agents

Mouna Abdessellem,^{†,‡} Markus Schoeffel,^{†,‡} Isabelle Maurin,[‡] Rivo Ramodiharilafy,[†] Gwennael Autret,[§] Olivier Clément,[§] Pierre-Louis Tharaux,[§] Jean-Pierre Boilot,[‡] Thierry Gacoin,[‡] Cedric Bouzigues,[†] and Antigoni Alexandrou^{*,†}

[†]Laboratoire d'Optique et Biosciences, Ecole Polytechnique, CNRS UMR 7645-INSERM U696, 91128 Palaiseau Cedex, France, [‡]Laboratoire de Physique de la Matière Condensée, Ecole Polytechnique, CNRS UMR 7643, 91128 Palaiseau Cedex, France, and [§]Paris Centre de Recherche Cardiovasculaire (PARCC), INSERM U970, 75015 Paris, France. [‡]These authors contributed equally.

ABSTRACT Collecting information on multiple pathophysiological parameters is essential for understanding complex pathologies, especially given the large inter-individual variability. We report here multifunctional nanoparticles which are luminescent probes, oxidant sensors, and contrast agents in magnetic resonance imaging (MRI). Eu^{3+} ions in a yttrium vanadate matrix have been demonstrated to emit strong, nonblinking, and stable luminescence. Time- and space-resolved optical oxidant detection is feasible after reversible photoreduction of Eu^{3+} to Eu^{2+} and reoxidation by oxidants, such as H_2O_2 , leading to a modulation of the luminescence emission. The incorporation of paramagnetic Gd^{3+} confers in addition proton relaxation enhancing properties to the system. We synthesized and characterized nanoparticles of either 5 or 30 nm diameter with compositions of GdVO_4 and $\text{Gd}_{0.6}\text{Eu}_{0.4}\text{VO}_4$. These particles retain the luminescence and oxidant detection properties of $\text{YVO}_4:\text{Eu}$. Moreover, the proton relaxivity of GdVO_4 and $\text{Gd}_{0.6}\text{Eu}_{0.4}\text{VO}_4$ nanoparticles of 5 nm diameter is higher than that of the commercial Gd^{3+} chelate compound Dotarem at 20 MHz. Nuclear magnetic resonance dispersion spectroscopy showed a relaxivity increase above 10 MHz. Complexometric titration indicated that rare-earth leaching is negligible. The 5 nm nanoparticles injected in mice were observed with MRI to concentrate in the liver and the bladder after 30 min. Thus, these multifunctional rare-earth vanadate nanoparticles pave the way for simultaneous optical and magnetic resonance detection, in particular, for *in vivo* localization evolution and reactive oxygen species detection in a broad range of physiological and pathophysiological conditions.



KEYWORDS: lanthanide nanoparticles · multifunctional probe · oxidant sensor · contrast agent · MRI

The design and tailoring of nanosized materials opened numerous perspectives in the biomedical field. In particular, their use as drug carriers enjoys increasing popularity because of their better pharmacokinetic properties compared to small-molecule-based drugs.¹ Moreover, nanomaterials allow for (i) multiple functionalizations and (ii) combined implementations of optical and magnetic properties which led to the development of novel combined imaging and therapy approaches including targeted drug delivery and medical imaging features. Such multimodal systems showed promising results for cancer treatment, and some of them are undergoing clinical studies (phase 1/2).²

Collecting information on multiple sources is essential in understanding specific pathophysiological processes in a living organism in their full complexity and consequently in enabling more accurate diagnosis and design of novel therapeutic approaches. Given the interindividual variability of pathophysiological parameters, detecting multiple signals in a single experiment is crucial. Additional benefits of multimodal probes arise from less toxicity as a lower amount of xenobiotics has to be injected and from cost reduction.² These features have led to widespread development of bi- or multifunctional biomedical imaging probes, especially those suitable for the most common modalities, such as fluorescence^{3,4} and magnetic resonance imaging (MRI).^{5–9}

* Address correspondence to antigoni.alexandrou@polytechnique.edu.

Received for review January 8, 2014 and accepted October 7, 2014.

Published online October 07, 2014
10.1021/nn504170x

© 2014 American Chemical Society

Aiming at the combination of the latter two modalities, a first approach consisted of covalently grafting a fluorescent moiety to a gadolinium chelate,^{10,11} Gd³⁺ ions being the most commonly used ions for T₁-based MRI contrast enhancement. Organic near-infrared fluorophores were also linked to superparamagnetic particles such as iron oxide nanoparticles (NPs),¹² which are routinely used as T₂-based MRI contrast agents.⁶ Quantum dots coated with paramagnetic lipids (PEGylated Gd-DTPA) and polyethylene glycol (PEG) were successfully used as dual-modality agents.¹³ Furthermore, Gd-based nanosized MRI contrast enhancers were functionalized with coatings containing organic fluorophores.¹⁴ Recent developments in this field led to the synthesis of all-in-one fluorescent and paramagnetic gadolinium-based nanoparticles.^{15–17} Stable luminescence properties originate from doping with rare-earth ions which provide a photostable, nonblinking, narrow emission.¹⁸ They may also exhibit up-conversion properties for excitation in the near-infrared range.^{17,19} Besides simply detecting the nanoparticles through their light emission, we have shown that Eu-doped nanoparticles can be used as oxidant sensors.²⁰ Reactive oxygen species (ROS) and more specifically hydrogen peroxide (H₂O₂) is produced as a secondary cellular messenger involved in a variety of signaling pathways^{21,22} including those resulting in cell contraction, migration, and cell injury and healing.^{23–25} Thus, H₂O₂ which was for a long time considered to be a lethal cellular waste is now attracting increasing interest. The quest for appropriate sensors, however, has been restricted by the requirement to provide simultaneously quantitative, time- and space-resolved, intracellular detection.^{26–29} In our previous work, we demonstrated that Eu-doped YVO₄ nanoparticles uniquely combine all these properties and can quantitatively probe local intracellular concentrations of H₂O₂ and their evolution in time.^{20,30} We have furthermore shown that these particles are ideal for single-molecule labeling and tracking and used them for the determination of confinement potentials in membrane lipid rafts.^{31,32}

Moreover, detecting reactive oxygen species concentration levels in living organisms is particularly important because ROS signaling and oxidative stress play a complex role in multiple pathologies. For instance, oxidative stress is an essential element in inflammatory processes^{25,33} and in neurodegenerative diseases, for example, in the degeneration of dopaminergic neurons in Parkinson's disease.³⁴ ROS further regulate the formation and the evolution of tumors:³⁵ cancer cells are indeed known to exhibit high levels of oxidative stress,³⁶ and ROS are involved in the triggering of tumoral transitions³⁷ but also control the activity of tumor suppressors.^{38,39} ROS concentration evolution might thus constitute a chemical signature of tumoral tissues and be an efficient diagnosis indicator.

More generally, precise determination of spatiotemporal patterns of ROS production is likely to provide significant improvement in the understanding of how ROS-related pathologies are triggered. Therefore, a multifunctional imaging probe that combines ROS detection with complementary modalities is highly desirable. Despite this, only few probes have been implemented for *in vivo* detection,^{29,40–42} and to our knowledge, no multifunctional probes including ROS detection capability exist.

Here, we propose a novel nanosized material which combines magnetic resonance contrast enhancing properties with luminescence properties and hydrogen peroxide sensing features. We designed a versatile luminescent MRI contrast enhancer based on Gd_{0.6}Eu_{0.4}VO₄ nanoparticles of 5 or 30 nm size. We demonstrated that these Eu-doped GdVO₄ particles retain the luminescence and hydrogen sensing properties of Eu-doped YVO₄²⁰ in the 1–100 μM range relevant for biological signaling. This novel paramagnetic system shows high relaxivities ($r_1 = 8.18 \text{ mM}^{-1} \text{ s}^{-1}$, $r_2 = 9.38 \text{ mM}^{-1} \text{ s}^{-1}$) and extremely low Gd³⁺ leaching. The relaxation enhancement induced by these nanoparticles is easily detected with magnetic resonance imaging in mice.

RESULTS AND DISCUSSION

Particle Size, Shape, and Microstructure. GdVO₄ and Eu-doped GdVO₄ nanoparticles of about 5 and 30 nm were synthesized using protocols already optimized for Y_{1-x}Eu_xVO₄ particles of similar size. The 30 nm particles were obtained by a standard coprecipitation route in water,⁴³ whereas the addition of citrate ions during the synthesis leads to the formation of smaller 5 nm particles.⁴⁴ The size obtained from dynamic light scattering measurements and the zeta-potential for both types of nanoparticles are reported in the Supporting Information Table S1. We analyzed the transmission electron microscopy (TEM) micrographs of over 400 GdVO₄ nanoparticles prepared by the standard route and found that their two-dimensional projection is an ellipse with the two major axes having lengths of 13.1 ± 1.1 and 26.6 ± 4.8 nm (mean \pm standard deviation), respectively (Figure 1A–C). High-resolution TEM images (Figure 1B) show local fluctuations of the contrast within a particle that may be due to particle porosity, to a nonsmooth surface texture, and/or to the presence of an internal substructure. However, even if several crystallites are present in each nanoparticle, they apparently retain a preferential crystallographic orientation as lattice fringes were found to extend over the whole particle.

This latter conclusion was confirmed by the analysis of X-ray diffraction (XRD) data, which give access to the structural coherence length or crystallite size (Supporting Information Figure S1). Complemented by Rietveld analysis, the microstructural study suggests

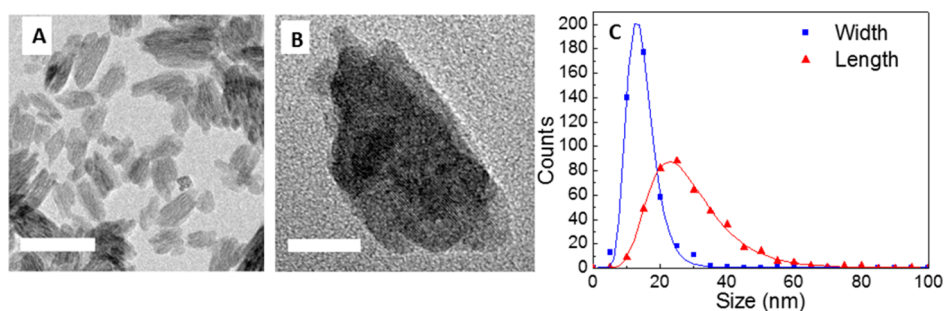


Figure 1. (A) TEM image of normal-route GdVO_4 nanoparticles, scale bar: 50 nm. (B) High-magnification TEM image, scale bar: 10 nm. (C) Width and length distributions obtained from 420 GdVO_4 particles. The solid lines are log-normal fits of the size distributions.

that the nanoparticles can be described as compressed prolate spheroids with 16 nm thickness and 25 nm length (Supporting Information Figure S1), in very good agreement with the dimensions found by TEM. This speaks either for an absence of internal substructure or for the presence of a 3D ordered polygranular substructure.

The high-resolution TEM images indicate a high specific surface, similarly to what was reported for $\text{Y}_{0.6}\text{Eu}_{0.4}\text{VO}_4$ samples synthesized with the same protocol and which show a similar microstructure.¹⁹ In addition, gas adsorption measurements on these Eu-doped YVO_4 nanoparticles analyzed with the Brunauer–Emmett–Teller theory showed that their specific surface was almost 20 times higher than the one expected from the geometric size of the particles.¹⁹ The high specific surface suggested by the high-resolution TEM images is probably related to the low (ambient) temperature of the synthesis and may play a key role in the sensing and relaxation properties of $\text{Gd}_{0.6}\text{Eu}_{0.4}\text{VO}_4$ by providing solvent access to a greater number of Eu^{3+} and Gd^{3+} ions.

The structural and microstructural characterization of the citrate-route nanoparticles is discussed in the Supporting Information. Briefly, TEM measurements yield a particle size of 5 ± 0.2 nm, and the X-ray diffraction analysis yields coherence length values ranging between 3 and 6 nm depending on the Bragg reflections.

After silica or dextran coating, the nanoparticles were characterized with Fourier transform infrared (FT-IR) spectroscopy measurements (Supporting Information Figure S3), which confirmed the efficiency of the coating procedures by detecting specific absorption peaks of Si–O–Si or C–H, C–O, and C–C bonds.

Luminescence and Hydrogen Peroxide Detection. The luminescence excitation and emission spectra of a suspension of $\text{Gd}_{0.6}\text{Eu}_{0.4}\text{VO}_4$ nanoparticles are shown in Figure 2A,B. $\text{Gd}_{0.6}\text{Eu}_{0.4}\text{VO}_4$ absorbs strongly in the UV range, and an efficient energy transfer is possible from VO_4^{3-} ions to Eu^{3+} ions.⁴⁵ The emission spectrum is similar to that measured for $\text{Y}_{0.6}\text{Eu}_{0.4}\text{VO}_4$ nanoparticles⁴³ and corresponds to that found for Eu-doped

GdVO_4 in the literature^{45,46} with a peak at 593 nm due to the $^5\text{D}_0\text{--}^7\text{F}_1$ transition, the strong principal double emission peak at 616 nm ($^5\text{D}_0\text{--}^7\text{F}_2$), a weak peak at 650 nm ($^5\text{D}_0\text{--}^7\text{F}_3$), and another double peak at 699 nm ($^5\text{D}_0\text{--}^7\text{F}_4$). A quantum yield of 3.8% was determined using rhodamine as a reference. Similar emission spectra are observed for direct excitation of the Eu^{3+} ions at 396 and 466 nm (Supporting Information Figure S4). We measured similar excitation and emission spectra for the citrate-route nanoparticles (Supporting Information Figure S5) and a quantum yield of 10%.

Solutions of 30 nm $\text{Gd}_{0.6}\text{Eu}_{0.4}\text{VO}_4$ nanoparticles were spin-coated on a glass coverslip after dilution to ensure single-particle imaging (Figure 2B) and illuminated at 466 nm at relatively high laser intensity (1.6 kW/cm^2). We observed a decrease of the luminescence after 250 s due to photoreduction of Eu^{3+} to Eu^{2+} similar to the one detected in Eu-doped YVO_4 .²⁰ The luminescence decrease is due to the fact that we detect the emission of Eu^{3+} ions with a filter centered at 617 nm, and the emission of Eu^{2+} is shifted to lower wavelengths.²⁰ Moreover, different single nanoparticles show a similar photoreduction and reoxidation behavior (Supporting Information Figure S6). The luminescence evolution averaged for 20 nanoparticles shows a biexponential decay during photoreduction ($T_1 = 3.6 \pm 0.1$ s and $T_2 = 49.7 \pm 2.5$ s) and a luminescence signal decrease of 30% (Figure 2C). The characteristic decay times and the signal decrease are comparable to those observed for $\text{Y}_{0.6}\text{Eu}_{0.4}\text{VO}_4$ nanoparticles²⁰ under a similar illumination. Upon addition of H_2O_2 , we observe a luminescence signal recovery due to chemical reoxidation of Eu^{2+} ions back to their initial Eu^{3+} state. Additions of H_2O_2 concentrations as small as $1 \mu\text{M}$ can be detected (Figure 2D). The final luminescence value after a photoreduction/chemical reoxidation cycle is a monotonous function of the H_2O_2 concentration (Figure 2D). $\text{Gd}_{0.6}\text{Eu}_{0.4}\text{VO}_4$ nanoparticles are thus efficient, quantitative oxidant local sensors in the physiological signaling range of $1\text{--}100 \mu\text{M}$ H_2O_2 . Note also that the photoreduction/reoxidation process is reversible rendering time-resolved detection possible (Supporting Information

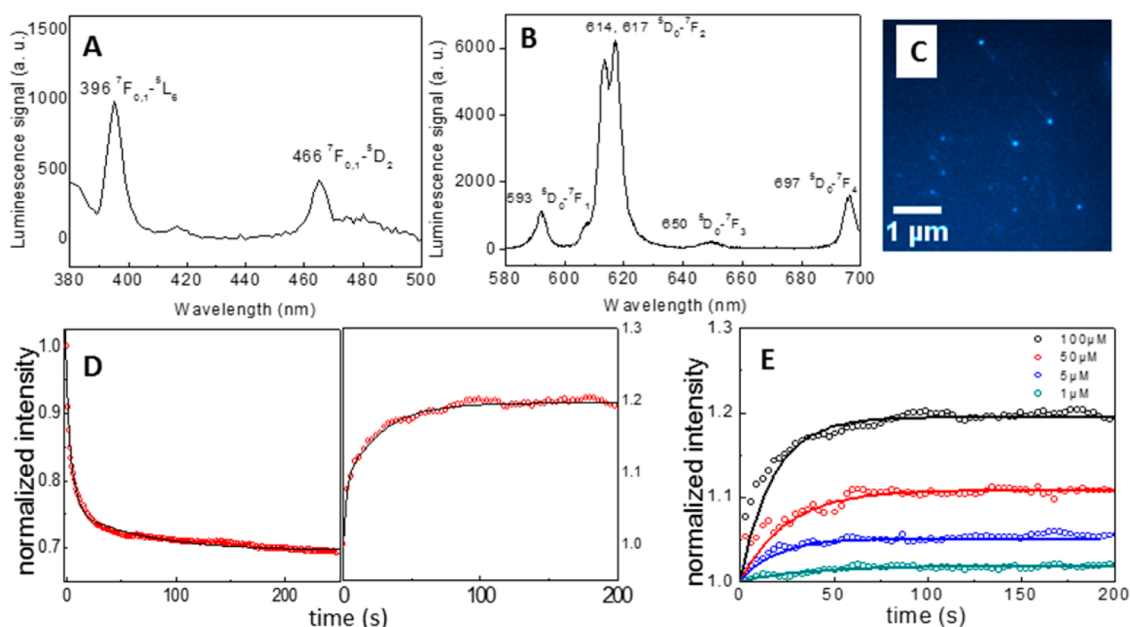


Figure 2. Luminescence and hydrogen peroxide detection properties of normal-route $\text{Gd}_{0.6}\text{Eu}_{0.4}\text{VO}_4$ nanoparticles. (A) Luminescence excitation spectrum (detection at 615 nm). (B) Emission spectrum (excitation at 280 nm). The peak positions as well as the corresponding transitions are indicated. (C) $\text{Gd}_{0.6}\text{Eu}_{0.4}\text{VO}_4$ NPs detected individually on a glass coverslip. Excitation at 466 nm, detection at 617 nm. Laser intensity: 1.6 kW/cm^2 ; acquisition time: 1 s. (D) Luminescence intensity evolution of a single nanoparticle. Left panel: Photoreduction under strong illumination (1.6 kW/cm^2 , excitation at 466 nm, detection at 617 nm) during $t = 250 \text{ s}$. Acquisition time: 1 s. Right panel: Excitation intensity was lowered to 0.3 kW/cm^2 , and $100 \mu\text{M}$ hydrogen peroxide was added to the medium (pure water) causing luminescence recovery. Acquisition time: 3 s. The luminescence decrease and recovery are fitted with a biexponential and a monoexponential, respectively (solid black lines). (E) Luminescence recovery averaged for ~ 20 individually detected nanoparticles for different hydrogen peroxide concentrations. Particles were photoreduced prior to H_2O_2 addition as shown in C. Laser intensity: 0.3 kW/cm^2 ; excitation at 466 nm; acquisition time: 3 s.

Figure S7). Moreover, the response to hydrogen peroxide in physiological medium reveals that it is affected neither by the presence of proteins nor by that of buffering ions (Figure S8). These properties are similar to those of $\text{Y}_{0.6}\text{Eu}_{0.4}\text{VO}_4$ particles^{20,21} and open the possibility of using Gd^{3+} -based nanoparticles for space- and time-resolved oxidant detection.

The oxidant sensing properties of citrate-route $\text{Gd}_{0.6}\text{Eu}_{0.4}\text{VO}_4$ nanoparticles are discussed in the Supporting Information (Figure S9). We found similar responses to hydrogen peroxide addition with a typical luminescence recovery of 8% after photoreduction and subsequent addition of $50 \mu\text{M}$ H_2O_2 . However, we observed a higher interparticle variability of the H_2O_2 -induced luminescence recovery (8% dispersion compared to 5% for 30 nm nanoparticles) and a slower recovery dynamics. These effects may be explained by the smaller size rendering the role of the surface more important or by differences of the surface properties due to the citrate complexes or of the crystallinity. This indicates that normal-route nanoparticles are a better choice for local hydrogen peroxide sensing at the cell level than citrate-route ones.

Relaxation Times at 20 MHz. Magnetization measurements carried out for both GdVO_4 and Eu-doped GdVO_4 nanoparticles indicate a paramagnetic behavior at room temperature. The main difference between bulk and

nanoparticle samples is a slight decrease of the exchange energy at low temperatures and a decrease of the paramagnetic to antiferromagnetic transition temperature (Supporting Information Figure S10). We determined the proton relaxation times of solutions of these rare-earth vanadate nanoparticles and found a linear dependence of the inverse relaxation times with the Gd^{3+} ion concentration contained in the respective particles for all examined samples. Data are shown for citrate-route $\text{Gd}_{0.6}\text{Eu}_{0.4}\text{VO}_4$ nanoparticles (Figure 3A), and the measured relaxivities for all studied samples are listed in Table 1. We paid particular attention to a precise measurement of the Gd^{3+} ion concentration (see Supporting Information) because it determines the precision of the relaxivity values. All samples show relaxivity ratios r_2/r_1 similar to those found for Dotarem and free Gd^{3+} ions of about 1.2 and are thus positive contrast agents.

Silica-coated nanoparticles compared to pristine ones show similar r_1^{ion} and r_2^{ion} relaxivity values (Table 1). We can thus conclude that the silica coating does not impede contact of water protons with the gadolinium ions, which is consistent with the fact that the silicate layer has been shown to be partially condensed and permeable to small molecules.^{20,47} This opens the way for further functionalization of the silica-coated particles which is required for active targeting.

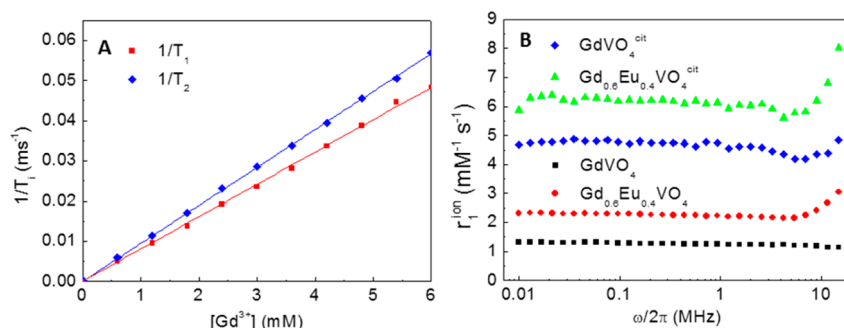


Figure 3. (A) Relaxation times for citrate-route $\text{Gd}_{0.6}\text{Eu}_{0.4}\text{VO}_4$ nanoparticles. The solid lines are linear fits to the data. (B) Comparison of the NMRD profiles for several Gd-containing nanoparticles. The superscript “cit” stands for particles synthesized by the citrate route.

TABLE 1. Relaxivities for Rare-Earth Vanadate Nanoparticles Measured at 20 MHz and 37 °C in Water^a

composition	d (n) (nm)	sample	r_1^{ion} ($\text{mM}^{-1} \text{s}^{-1}$)	r_2^{ion} ($\text{mM}^{-1} \text{s}^{-1}$)	r_1^{NP}	r_2^{NP}	r_2/r_1
GdVO_4	41	this work	0.95	1.31	420000	570000	1.08
$\text{Gd}_{0.6}\text{Eu}_{0.4}\text{VO}_4$	42	this work	2.97	3.47	840000	980000	1.17
$\text{Gd}_{0.6}\text{Eu}_{0.4}\text{VO}_4/\text{SiO}_2$	57	this work	2.52	3.03	710000	860000	1.20
$\text{GdVO}_4^{\text{cit}}$	11	this work	4.60	5.52	390000	470000	1.20
$\text{Gd}_{0.6}\text{Eu}_{0.4}\text{VO}_4^{\text{cit}}$	14	this work	8.18	9.38	860000	980000	1.15
Dotarem	CC	Guerbet	3.59	4.44			1.23
GdCl_3	ion	Prolabo	10.4	12.1			1.16

^a Particle sizes are given as the number-average diameter from dynamic light scattering measurements. r_i^{ion} is the relaxivity relative to the molar quantity of Gd^{3+} ions. Given the fact that the Eu^{3+} ions also contribute to the relaxivity (see below), the relaxivity values of Eu-doped nanoparticles relative to the molar quantity of both rare-earth ions (Gd^{3+} and Eu^{3+}) can be obtained from the values of the table by multiplying with 0.6. The relaxivity for an average nanoparticle is denoted by r_i^{NP} ($i = 1, 2$). The superscript “cit” denotes nanoparticles formed *via* the citrate route. CC stands for coordination complex.

In the case of $\text{GdVO}_4^{\text{cit}}$ and $\text{Gd}_{0.6}\text{Eu}_{0.4}\text{VO}_4^{\text{cit}}$ nanoparticles, we find relaxivities higher than the relaxivities of the commercial compound Dotarem (Table 1). A comparison of the samples $\text{GdVO}_4^{\text{cit}}$ to GdVO_4 and $\text{Gd}_{0.6}\text{Eu}_{0.4}\text{VO}_4^{\text{cit}}$ to $\text{Gd}_{0.6}\text{Eu}_{0.4}\text{VO}_4$, shows that relaxivity values per Gd^{3+} ion are higher for the smaller particles prepared by the citrate route. *A priori*, according to the Solomon–Bloembergen equations^{9,48} for the proton relaxation in the presence of a contrast agent, this dependence with the particle size results from the interplay between two quantities: (i) the number of accessible Gd^{3+} ions and (ii) the rotational correlation time of the contrast agent.

Indeed, the proton relaxation times according to the Solomon–Bloembergen equations^{9,48} strongly depend on τ_{ci} ($i = 1, 2$ for the longitudinal and transverse component), the dipole–dipole interaction time, given by the following equation:

$$\frac{1}{\tau_{ci}} = \frac{1}{\tau_M} + \frac{1}{T_{ei}} + \frac{1}{\tau_R} \quad (i = 1, 2) \quad (1)$$

where τ_M is the mean residence time of the bound water molecule, T_{ei} is, respectively, the longitudinal and transverse electron-spin relaxation time, and τ_R is the rotational correlation time. It is well-established for Gd chelates, at 20 MHz, that relaxivity increases in the same fashion as the rotational correlation time, that is, as the chelate size.⁴⁹ This trend, however, is no longer

valid for species with τ_R values above 10 ns where the third term in eq 1 becomes negligible and the electron-spin relaxation and/or residence lifetime terms become dominant.^{48,49} For spherical nanoparticles with a diameter $d = 12$ nm at 25 °C in water with a viscosity of $\eta \approx 0.9$ mPa·s,⁵⁰ we obtain $\tau_R = 200$ ns (in contrast, τ_R for Dotarem is only 80 ps⁵¹). Assuming that the surface Gd^{3+} ions in GdVO_4 particles retain the same electronic and water coordination properties as in Gd^{3+} chelates, the previous discussion suggests that τ_R only weakly influences the relaxivity of our samples. Thus, the higher relaxivity measured in the smaller NPs may result from a greater number of accessible Gd^{3+} sites in citrate-route particles. This number scales as the surface to volume ratio (*i.e.*, as $1/d$ for spherical NPs). This justifies quite well the difference observed between $\text{Gd}_{0.6}\text{Eu}_{0.4}\text{VO}_4$ and $\text{Gd}_{0.6}\text{Eu}_{0.4}\text{VO}_4^{\text{cit}}$, where the diameter ratio of 3 (42 nm/14 nm) is consistent with the relaxivity ratios of $8.18/2.97 = 2.75$ and $9.38/3.47 = 2.70$, respectively, for r_1 and r_2 (see Table 1). Moreover, changes in relaxivity between the two different synthesis routes may also result from a different degree of porosity and/or from different surface states (including surface charge and solvation shell structure) and thus different accessibility to Gd^{3+} ions. Given that smaller nanoparticles exhibit higher relaxivity values per Gd^{3+} ion and assuming that the toxicity of the nanoparticles is only determined by the total Gd^{3+} quantity

administered to the patient, it is thus preferable to introduce more nanoparticles of smaller size for a given quantity of material.

Interestingly, in $\text{Gd}_{0.6}\text{Eu}_{0.4}\text{VO}_4$ and $\text{Gd}_{0.6}\text{Eu}_{0.4}\text{VO}_4^{\text{cit}}$ nanoparticles, replacing the paramagnetic Gd^{3+} ions by the nonmagnetic Eu^{3+} ions does not diminish proportionally the relaxivity of these compounds compared to Gd-based nanoparticles (Table 1). We therefore examined the contribution of Eu^{3+} to the relaxivity with frequency-dependent relaxation measurements.

Frequency-Dependent Relaxation Times. Longitudinal relaxation times were measured as a function of the Larmor frequency in the range from $\omega/2\pi = 10$ kHz to 15 MHz (2.3 mT to 0.35 T). The corresponding Gd^{3+} concentration normalized relaxivities are plotted in Figure 3B for GdVO_4 nanoparticles, doped or not with Eu^{3+} , from the normal and citrate routes. The relaxivities are nearly constant for all samples up to a frequency of about 5 MHz. A similar behavior was also found for Gd^{3+} chelates where the plateau range extends up to 1–10 MHz depending on the actual contrast agent.⁹ For high frequencies beyond the plateau range, the relaxivity decreases dramatically for Gd chelates, such as Dotarem, from 1 to 10 MHz,⁹ whereas the relaxivities for our Eu-doped nanoparticles are constant from 0.01 to 10 MHz with an increase setting in for frequencies above 10 MHz for all nanoparticles except normal-route GdVO_4 (Figure 3). This difference in frequency dependence between Gd chelates and nanoparticles can be explained by the difference in rotational correlation time and corresponds to the predictions of Lauffer *et al.*^{9,48} Indeed, Lauffer predicts a relaxivity maximum between 10 and 100 MHz for long rotational correlation times.⁴⁸ These calculations were done for rotational correlation times of $\tau_R = 20$ ns; however, as indicated above, the effect of the rotational correlation time on the relaxivity behavior becomes negligible for τ_R values above 10 ns. As commercial MRI scanners operate at a magnetic field of 1.5 T or now also 3 T, corresponding respectively to a proton resonance frequency of 64 or 128 MHz, a contrast agent that shows a marked relaxation maximum in this range is of great interest.

These data confirm the trends observed at a single frequency (20 MHz, Table 1). Over the whole frequency range, the suspensions containing nanoparticles from the citrate route show higher relaxivities than those obtained from the normal synthesis path. Furthermore, Eu-containing nanoparticles possess a higher r_1 relaxivity than those without Eu for all measured frequencies. Trivalent europium ions at the ground state are not expected to influence the magnetic properties of the nanoparticles as $J = 0$ (Eu^{3+} , $4f^6$, $L = S = 3$). However, the energy separation between the ground state and the first excited state is only 255 cm^{-1} ,⁵² which is comparable to the energy kT corresponding to the measurement temperature, 37 °C. This peculiar

configuration results in the so-called Van Vleck paramagnetism⁵² that predicts a nonzero magnetic moment of trivalent europium ions at room temperature. The effective magnetic moment at 300 K of Eu^{3+} -based materials shows values of approximately $3.4 \mu_B$ (Bohr magneton) per Eu^{3+} ion depending on the oxide.^{50,51} The moment of Gd^{3+} -based nanoparticles is $7.9 \mu_B$ per Gd^{3+} ion ($J = S = 7/2$). We can thus estimate the squared magnetic moment of $\text{Gd}_{0.6}\text{Eu}_{0.4}\text{VO}_4$ particles by adding the weighted contributions of Eu and Gd trivalent ions which yields an effective squared magnetic moment of $42 \mu_B^2$ per rare-earth ion.

Therefore, reporting the relaxivity per Gd^{3+} ion and neglecting the contribution of Eu^{3+} ions to the magnetic moment, and thus to the relaxivity, leads to an overestimation of the r_1^{ion} and r_2^{ion} relaxivity values for nanoparticles containing 40% of Eu^{3+} ions. It is well-known that the inner-sphere contribution to the relaxation times and thus the relaxivities depends on the effective magnetic moment as follows: $1/T_i^{\text{DD}} \propto g^2 \mu_B^2 S(S+1) = \mu_{\text{eff}}^2$, where T_i^{DD} refers to the longitudinal and transverse dipole–dipole relaxation times, g is the electronic Landé factor, μ_B the Bohr magneton, S the spin number, and μ_{eff} the effective magnetic moment.⁹ For citrate-route nanoparticles, the relaxivity values below 1 MHz are $6.4 \text{ mM}^{-1} \text{ s}^{-1}$ for the Eu-doped NPs relative to the molar quantity of Gd^{3+} ions (*i.e.*, $3.8 \text{ mM}^{-1} \text{ s}^{-1}$) relative to the molar quantity of both rare-earth ions (Gd^{3+} and Eu^{3+}) and $4.6 \text{ mM}^{-1} \text{ s}^{-1}$ for the nondoped NPs. The relaxivity ratio is thus $4.6/3.8 = 1.2$, which is compatible with the ratio of the squared effective magnetic moments: $(\mu_{\text{GdVO}_4}^2)/(\mu_{\text{Gd}_{0.6}\text{Eu}_{0.4}\text{VO}_4}^2) = (62/42)^2 = 1.5$. This clearly demonstrates the contribution of Eu^{3+} ions in the relaxation properties of $\text{Gd}_{0.6}\text{Eu}_{0.4}\text{VO}_4$.

Assessment of Rare-Earth Leaching from Nanoparticles.

Free rare-earth ions are cytotoxic, and the median lethal dose (DL_{50}) in mice is 100–200 and 550 mg/kg for GdCl_3 ^{53,54} and EuCl_3 ,⁵⁵ respectively. We therefore measured the kinetics of rare-earth leaching from a dispersion of normal-route $\text{Gd}_{0.6}\text{Eu}_{0.4}\text{VO}_4$ nanoparticles in ultrapure water using xlenol orange to detect the free rare-earth concentration for an initial nanoparticle concentration corresponding to 67 mM in vanadate ions (Figure 4). To assess the free rare-earth concentration, we centrifuged to separate the nanoparticles and then titrated the free rare-earth ions in the supernatant (Methods in the Supporting Information). We performed, after synthesis, five purification cycles to remove most of the unreacted rare-earth ions. The decrease in rare-earth concentration after each washing step shows their clearance from the solution (Figure 4). Moreover, the relatively slow decrease suggests that not only unreacted rare-earths in solution but also adsorbed rare-earth ions at the nanoparticle surface are removed. These adsorbed species have been observed at the surface of lanthanide

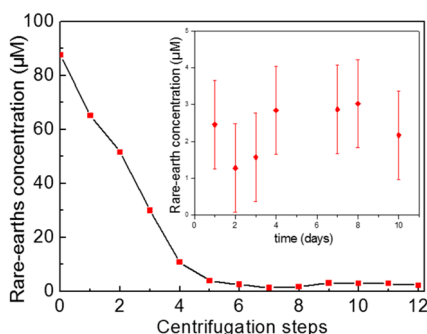


Figure 4. Concentration in free rare-earth ions after successive centrifugation steps to remove unreacted precursors after a normal-route synthesis for an initial rare-earth concentration of 67 mM in vanadate ions. The solid line is a guide for the eye. Inset: Rare-earth concentration as a function of the time separating two purification steps after the removal of residual unreacted species.

vanadates⁵⁶ and could contribute to particle stability in solution. Further centrifugation steps do not lead to a further decrease of the residual free rare-earth concentration which remains stable at approximately $2\ \mu\text{M}$ for normal-route particles (Figure 4). The detected value of $2\ \mu\text{M}$ represents ~ 30 ppm of the total rare-earth ion content in the nanoparticles. We then performed another series of experiments at room temperature, after the initial purification cycles, where centrifugations were performed after a variable number of days up to 10 days. After each centrifugation, the rare-earth concentration in the supernatant was assessed (inset Figure 4); no increase of free rare-earth ions in solution was observed. Similar measurements over a period of 10 days at room temperature for citrate-route nanoparticles (initial concentration of 67 mM in vanadate ions) led to rare-earth concentration values below our detection limit ($-1.6 \pm 2.6\ \mu\text{M}$). Note, however, that rare-earth leaching may be higher in biological environments, in particular, due to the presence of Ca^{2+} ions and to transmetalation reactions. The potential role of this effect will be addressed in future work.

Moreover, free vanadate ions have also been shown to be carcinogenic due to interference with redox regulation and signaling pathways through interaction with phosphate binding sites of protein phosphatases.⁵⁷ A significant number of deaths were found in mice for sodium orthovanadate doses higher than 30 mg/kg/day.⁵⁸ Given the fact that vanadate ions are released from the solid matrix where they are present in the same concentration as rare-earth ions, we may assume that they are released in equally small concentrations.

We thus demonstrated negligible rare-earth leaching from the Eu-doped GdVO_4 particles for both synthesis routes, significantly smaller than the values reported in the literature. For comparison, Hifumi *et al.*⁵⁹ reported for dextran-coated GdPO_4 nanoparticles, with an initial concentration of 2.2 mM in Gd^{3+}

ions, a leached concentration of $6.5\ \mu\text{M}$ after 2 weeks at $4\ ^\circ\text{C}$ (which corresponds to 3000 ppm), and Huang *et al.*⁶⁰ found 33 and $43\ \mu\text{M}$ of free gadolinium after 8 days at $37\ ^\circ\text{C}$ for hollow and porous Gd_2O_3 nanoparticles with an initial concentration of 2.2 mM in Gd^{3+} ions, respectively (corresponding to 15 000 ppm and 19 500 ppm, respectively). Given their good relaxivity properties and their very low leaching, these $\text{Gd}_{0.6}\text{Eu}_{0.4}\text{VO}_4$ nanoparticles are suitable for *in vivo* injections and are expected to produce contrast enhancement in MRI.

Toxicity Measurements. We evaluated the potential cell mortality induced by incubation with dextran-coated nanoparticles at a similar concentration ($200\ \mu\text{L}$ at 10 mM in vanadate ions added to 2 mL of culture medium) as the one resulting from nanoparticle injection ($200\ \mu\text{L}$ at 10 mM in vanadate ions) in the mouse blood circulation, assuming a blood volume of 2 mL. We used endothelial progenitor cells (EPCs), which are endothelial cells likely to encounter intravenously injected xenobiotics. Cell mortality MTT tests (see Methods in the Supporting Information) on EPCs showed no cytotoxicity of citrate-route $\text{Gd}_{0.6}\text{Eu}_{0.4}\text{VO}_4$ particles after 3 h and overnight incubation ($102 \pm 5\%$ and $99 \pm 3\%$ versus $100 \pm 3\%$ for control cells). Normal-route particles induced limited cell death (13% after 3 h and 25% after an overnight incubation, Supporting Information Figure S11). These results indicate a reasonable tolerance of $\text{GdVO}_4\text{:Eu}$ nanoparticles, notably of citrate-route nanoparticles, which are more suitable for *in vivo* experiments.

MRI. We injected dextran-coated citrate-route $\text{Gd}_{0.6}\text{Eu}_{0.4}\text{VO}_4$ nanoparticles antero-orbitally into three BL6 mice and monitored the MRI contrast enhancement for 2 h. During all experiments, all physiological constants (breathing and heart rate) of injected mice remained normal, indicating the absence of harmful effects of $\text{Gd}_{0.6}\text{Eu}_{0.4}\text{VO}_4$ nanoparticles. T_1 -weighted MRI images demonstrate that the $\text{Gd}_{0.6}\text{Eu}_{0.4}\text{VO}_4$ colloid is an efficient contrast enhancer as significant signal changes up to 45% were measured after injection of 0.06 mmol/kg $\text{Gd}_{0.6}\text{Eu}_{0.4}\text{VO}_4$ (the value indicated corresponding to that for Gd^{3+} ions), an amount typical of that used for experiments with Dotarem (usual recommended dose of Dotarem is 0.1 mmol/kg). Monitoring of the bladder areas showed a signal increase during the first 30 min after injection, which we attribute to an accumulation of the nanoparticles in the bladder (Figure 5B,C). This means that the circulation time of the nanoparticles in mouse blood is at least 30 min. For comparison, Dotarem typical circulation time is 10 min approximately.⁶¹ Moreover, during our observation time, the volume of the bladders increased and their shapes tended to change from round to ellipsoidal. Considering that the third dimension of the bladder is equal to the average of the two axes of the ellipse observed in the 2D projection, we find an average

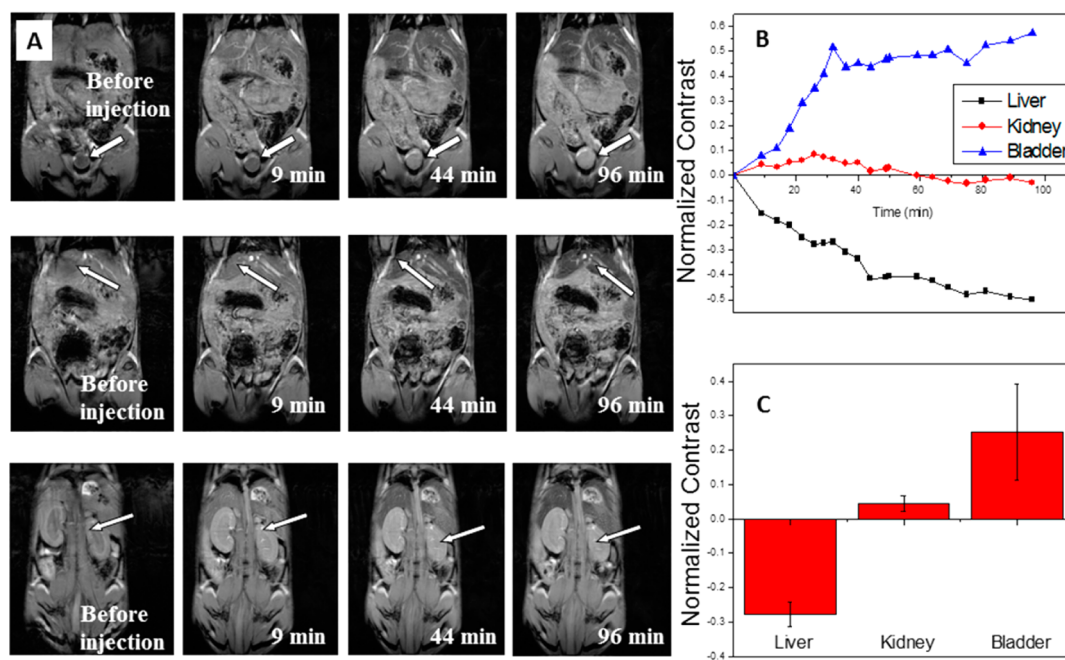


Figure 5. (A) T_1 -weighted MRI monitoring at different times before and after 0.06 mmol/kg injection of dextran-coated citrate-route $Gd_{0.6}Eu_{0.4}VO_4$ nanoparticles. The three rows correspond to a selection of coronal planes of the mouse. White arrows show organs of interest. (B) Contrast evolution in bladder, liver, and kidney after injection of the nanoparticles for the mouse shown in (A). The signal was averaged over the area of the organ of interest and normalized to the reference signal of a phantom tube containing water. (C) Signal evolution 30 min after injection averaged for three mice. Error bars are standard error of the mean.

volume increase of $80 \pm 54\%$ for the three mice injected with citrate-route $Gd_{0.6}Eu_{0.4}VO_4$ nanoparticles probably due to the liquid injected.

In the liver, we observe a signal decrease (instead of an increase) of 45% which is most probably due to rapid uptake of large amounts of NPs (Figure 5C). For large NP concentrations, the contrast agent accumulation causes local field heterogeneities which result in the so-called T_2^* artifact, that is, a decrease of the transverse (T_2) relaxation time of protons in this organ leading to a decrease of the signal in T_1 -weighted MRI images.^{17,62,63} This hypothesis is confirmed by luminescence measurements that show the characteristic red luminescence of $Gd_{0.6}Eu_{0.4}VO_4$ in extracted liver tissue homogenates (see Supporting Information Methods and Figure S12). The signal in the kidneys remains stable over the monitoring time, which suggests that nanoparticles do not accumulate in this organ.

Note that the nanoparticle uptake in the liver is faster than the arrival in the bladder (average characteristic times of 21 ± 9 min versus 37 ± 9 min). This is due to the different uptake mechanisms involved. Nanoparticle uptake in the liver is based on vascular diffusion followed by endocytosis and phagocytosis by Kupfer cells. Filtration by the kidney, however, requires several circulation cycles before the whole concentration is eliminated toward the bladder. Provided their size is small enough, typically only 20% of the nanoparticles will be filtered by the first passage through the kidneys.⁶⁴

We also performed an injection of 0.06 mmol/kg of normal-route $Gd_{0.6}Eu_{0.4}VO_4$ particles in the same conditions as above (Supporting Information Figure S13). Thirty minutes after injection, no contrast changes were measured in the bladder and kidneys, whereas we observed an important signal decrease (-55%) in the liver.

Luminescence detection in tissue homogenates confirms the presence of NP accumulation in the liver and the absence of nanoparticles in urine and kidneys (Supporting Information Figure S12). These experiments show that citrate-route nanoparticles are detected both in the urine and in the liver, whereas normal-route particles are only detected in the liver. This means that the smaller particles are at least partly cleared by the kidney and the bladder, whereas bigger particles are eliminated from the blood circulation into the liver because of the glomeruli filtering threshold.

These results are in agreement with the data reported in the case of quantum dots, where efficient and rapid uptake in the mouse bladder followed by urinary excretion and elimination was found to take place for nanoparticles with hydrodynamic diameters smaller than 5.5 nm.⁶⁵ For larger diameters, accumulation in the liver and other organs was observed.

CONCLUSIONS

We have synthesized nanoparticles made of pure $GdVO_4$ and $Gd_{0.6}Eu_{0.4}VO_4$ compositions. On the basis of well-documented synthesis routes, we produced for the two compositions nanoparticles of 5 and 30 nm

diameter. A combination of X-ray diffraction and electron microscopy experiments showed that the latter synthesis route yields GdVO_4 nanoparticles with a shape best described as compressed prolate spheroids with about 25 nm length and 16 nm height. TEM observations suggest that these particles have an internal structure which allows access of the solvent to Eu^{3+} and Gd^{3+} surface ions and thus favors both oxidant sensing and MRI contrast enhancement.

We have demonstrated that $\text{Gd}_{0.6}\text{Eu}_{0.4}\text{VO}_4$ nanoparticles retain the property of luminescence modulation by the oxidant concentration and thus allow quantitative, time- and space-resolved detection of intracellular H_2O_2 . Quantitative ROS detection using these probes inside living organisms should prove to be a valuable tool for assessing critical parameters of various ROS-related pathologies.

The advantage of gadolinium ions being incorporated as an integral component of the nanoparticle crystal structure lies in a very low leaching of free ions over a period of 10 days at room temperature. These particles are more stable than other MRI contrast enhancement particles reported in the literature.

We found that the relaxivity of pure or Eu-doped 5 nm GdVO_4 nanoparticles is higher than that of the commercial chelate compound Dotarem, making them promising candidates for biomedical applications. In addition, relaxivities for nanoparticle dispersions increase in the frequency range of interest for medical imaging while those of commercial gadolinium chelates decrease steeply. MRI imaging in mice

showed accumulation of the particles in the bladder and in the liver. A full biodistribution study of the nanoparticles will be performed in future work.

In conclusion, rare-earth vanadate nanoparticles containing simultaneously europium and gadolinium ions are multifunctional probes allowing detection of their localization using luminescence and MRI as well as detection of ROS concentrations produced in physiological or pathophysiological conditions. We demonstrated these multiple modalities for two different synthesis methods: the so-called normal and citrate synthesis path. Resulting nanoparticles retained these multicontrast abilities for biological imaging, even though they do not present the same performances for each modality. Citrate-route particles seem indeed more suitable for MRI, while ROS detection in cell culture is more efficient with normal-route nanoparticles. We thus have the possibility to choose between these different types of particles for further applications, in order to optimize multimodal imaging depending on the studied biological systems.

The Eu^{3+} excitation wavelength at 466 nm limits the optical imaging depth *in vivo* because of tissue absorbance. Nevertheless, ROS detection in superficial lesions or optical-fiber-based endoscopy at lesion sites remains possible and is highly relevant for numerous pathologies. Future work will exploit these multimodality features to detect recruitment dynamics of macrophages loaded with these particles to inflammation sites combined with the evaluation of the role of oxidative stress in this pathology.

EXPERIMENTAL METHODS

Nanoparticle Synthesis. Rare-earth vanadate nanoparticles were synthesized using two well-documented procedures, namely, standard coprecipitation⁴³ and citrate-assisted⁴⁴ routes, yielding particles of approximately 30 and 5 nm in size, respectively. Details are reported in the Supporting Information.

Silica Coating. Nanoparticles prepared through the standard or citrate routes were diluted in ultrapure water to a vanadate concentration of about 20 mM, and the dispersions were sonicated for several minutes. Then, the same volume of a 3 wt % sodium silicate solution (Na_2SiO_3 , Riedel-de Haën) was immediately added under vigorous stirring. The mixture was stirred overnight at ambient temperature and then dialyzed in Spectra Por regenerated cellulose dialysis membranes (MWCO 12–14 kDa) against ultrapure water for several days. Dialysis was stopped after reaching a conductivity of the nanoparticle dispersion between 50 and 100 $\mu\text{S}/\text{cm}$. The presence of a silica coating was validated by IR spectroscopy.

Dextran Coating. Nanoparticles were alternatively coated with carboxymethyl-dextran (CM-dextran) following the procedure described by Dutz *et al.*⁶⁶ colloidal solutions of 20 mM vanadate concentration were heated at 45 °C under vigorous stirring. CM-dextran powder (40 000 kDa, Sigma-Aldrich) was added in a dextran/nanoparticle mass proportion of 2:1. After 60 min condensation, the solutions were purified by successive centrifugations. The hydrodynamic radius of these nanoparticles before and after CM-dextran coating was measured by dynamic light scattering to be 23 and 35 nm (number-average values), respectively.

Standard Characterizations. Dynamic light scattering measurements were performed using a Malvern Nano ZS Zetasizer on diluted dispersions in water (25 °C, 633 nm). For all rare-earth vanadate materials, the refractive index was assumed to be the same as that of YVO_4 , that is, 1.99 at 25 °C and 633 nm.⁶⁷

For observations by transmission electron microscopy, we used dilute solutions of nanoparticles deposited on a carbon grid. Imaging was performed with a Philips CM30 microscope operating at 300 kV with a point resolution of 0.235 nm. Images were analyzed using the ImageJ software by manual selection.

X-ray powder diffraction measurements were recorded in Bragg–Brentano parafocusing geometry using a X'Pert MPD powder diffractometer ($\lambda = 1.5418 \text{ \AA}$). Diffracted intensity was monitored using an X'Celerator area detector (PANalytical) which covers a scattering angle segment of 2.546° through a nickel filter. Sample eccentricity and peak positions were calibrated using bulk GdVO_4 . Details related to the microstructural analysis of these XRD data are reported as Supporting Information.

Magnetization measurements were performed using a cryogenic SX600 magnetometer (see Supporting Information Figure S4). Powder samples were mounted in polycarbonate capsules with the powder blocked by paraffin wax. Magnetic data were systematically corrected for the diamagnetic contributions of the wax and polycarbonate capsule.

We performed FT-IR spectroscopy to characterize nanoparticle coatings with silica or dextran. A drop of colloid was deposited on a piece of silicon wafer and dried at 90 °C for several hours. The spectrum was measured with a Bruker Equinox infrared spectrometer from 500 to 4000 cm^{-1} . Data

were normalized to a reference silicon substrate (see Supporting Information Figure S2).

Luminescence Spectroscopy. Luminescence excitation and emission spectra were recorded using a Hitachi F-4500 fluorescence spectrophotometer with 2.5 nm spectral resolution. For excitation spectra, luminescence was excited in the wavelength range of 250–600 nm and emission was collected at 617 nm. For emission spectra, luminescence was excited at 280 nm. The luminescence quantum yield was determined by comparison of the spectrally integrated emission intensity to that of rhodamine 6G ($Q = 94\%$ in ethanol) in the wavelength range of 500–750 nm after excitation at 280 nm for solutions having similar optical density ($OD < 0.3$). We obtained the colloid quantum yield as follows: $Q_{NP} = (n_{NP}^2/n_R^2) \times (I_{NP}/I_R) \times (A_R/A_{NP})$, where n is the refractive index, I is the emission intensity, and A is the absorbance of the solutions.

Luminescence Microscopy Imaging. Single nanoparticle observation relies on the direct excitation of Eu^{3+} ions.²⁰ Imaging is carried out on an inverted microscope (Axiovert S100TV Carl Zeiss) under wide-field illumination by an Innova 300 argon ion laser (Coherent) at 466 nm. Nanoparticle luminescence is collected by an Apochromat 63 \times , 1.40 numerical aperture oil-immersion objective (Zeiss) and selected by a 500DCLP dichroic mirror (Chroma Technology) and a D617/8m band-pass filter (fwhm 8 nm, Chroma). Image acquisition is performed by a QuantEM 5125C CCD camera (Photometrics). Diluted solutions of nanoparticles are spin-coated on glass coverslips previously cleaned in a plasma cleaner. Their response to hydrogen peroxide is assessed as follows: the nanoparticles are photo-reduced at a laser intensity of 1.6 kW/cm² for 5 min (acquisition rate: 1 image/s). The stability of the luminescence level after photoreduction is checked at a laser intensity of 0.3 kW/cm² for 5 min (acquisition rate: 1 image every 3 s). The luminescence recovery is observed after addition of hydrogen peroxide (Sigma-Aldrich) in the solution for several minutes at a laser intensity of 0.3 kW/cm² (acquisition rate: 1 image every 3 s).

Measurement of Relaxation Times. Relaxation times were determined using a Bruker NMS 120 minispec relaxometer operating at a proton resonance frequency of $\omega/2\pi = 20$ MHz (0.47 T) and at 37 °C. T_1 relaxation times were determined from the inversion recovery pulse sequence with a repetition time $TR = 5$ s. The pulse separation time TI was adjusted until the condition $TI \approx 0.6 T_1$ was fulfilled. To measure the T_2 relaxation time, the Carr–Purcell–Meiboom–Gill pulse sequence was employed using a repetition time $TR = 8$ s. Generally, 100 echoes with an echo time TE between 0.5 and 2 ms depending on the concentration of the sample were recorded. TE was adjusted manually in order to record the complete magnetization decay during the 100 echoes.

Nuclear Magnetic Resonance Dispersion Spectroscopy. ¹H nuclear magnetic resonance dispersion (NMRD) spectroscopy experiments were carried out with a Stellar Spinmaster FFC2000 fast field cycling relaxometer at 25 °C. Relaxation times were measured in the 10 kHz to 15 MHz frequency range for a vanadate concentration of 10 mM. A polarization field corresponding to 15 MHz was applied for 2 s. The transition to the relaxation field was performed within 2 ms, and the magnetization relaxed for a time span Δ varied within the interval 0–5 T_1 . The remaining magnetization after Δ was measured after a quick transition within 1 ms to the acquisition field corresponding to 9 MHz and by applying a $\pi/2$ detection pulse.

In Vivo MRI. *In vivo* experiments were performed on BL6 wild-type mice anesthetized by isoflurane inhalation. Respiration was monitored during experiments, and isoflurane delivery was adjusted as a consequence to preserve stable vital signs in animals. Prior to contrast agent ($\text{Gd}_{0.6}\text{Eu}_{0.4}\text{VO}_4$) injection, we performed a first image series that represents the innate tissue contrast (measurement at time zero). T_1 -weighted imaging was performed with a BioSpec Bruker 47/40 USR apparatus at a field of 4.7 T and a corresponding frequency of 200 MHz. The parameters of the gradient echo sequence and the imaging configuration are as follows: $TR/TE = 150/5.4$ ms, $\alpha = 40^\circ$, $FOV = 5 \times 4$ cm, detection matrix = 256×256 , $NEX = 4$, slice thickness = 1 mm. The signal was measured in the liver, kidney, and bladder and normalized to a reference region (tube containing

water). Animals received humane care, and the study protocols complied with PARCC guidelines for the care and use of laboratory animals.

Conflict of Interest: The authors declare no competing financial interest.

Acknowledgment. The research described here has been partly supported by Triangle de la Physique (Contract 2008-051T). We are indebted to Pierre Levitz (LPMC) for the frequency-dependent measurements. We acknowledge financial support from CNRS Défi G3N 2012 and CNRS Défi Nano 2014.

Supporting Information Available: Dynamic light scattering and zeta-potential data for all samples mentioned, microstructural analysis for normal-route nanoparticles, structural characterization by TEM imaging and X-ray diffraction for citrate-route nanoparticles, infrared spectroscopy characterization of silica and dextran surface coatings, magnetic characterization of GdVO_4 and $\text{Gd}_{0.6}\text{Eu}_{0.4}\text{VO}_4$ NPs. Information is also given on the luminescence properties, the photoreduction and oxidant sensing capabilities of individual nanoparticles and of nanoparticle assemblies for citrate- and normal-route particles, the reversibility of the photoreduction/reoxidation reaction and the absence of modification of the oxidant sensing response in physiological medium. We also provide cell viability assay results, MRI measurements after injection of 30 nm $\text{Gd}_{0.6}\text{Eu}_{0.4}\text{VO}_4$ NPs, and luminescence measurements on urine, kidney, and liver tissue homogenates after NP injection. Finally, further description is given on experimental procedures for nanoparticle synthesis and purification, the determination of vanadate concentration, rare-earth leaching in solution, cell viability experiments, and luminescence imaging of tissue homogenates. This material is available free of charge via the Internet at <http://pubs.acs.org>.

REFERENCES AND NOTES

- Malam, Y.; Loizidou, M.; Seifalian, A. M. Liposomes and Nanoparticles: Nanosized Vehicles for Drug Delivery in Cancer. *Trends Pharmacol. Sci.* **2009**, *30*, 592–599.
- Cheng, Z.; Al Zaki, A.; Hui, J. Z.; Muzykantov, V. R.; Tsourkas, A. Multifunctional Nanoparticles: Cost versus Benefit of Adding Targeting and Imaging Capabilities. *Science* **2012**, *338*, 903–910.
- Goldys, E. *Fluorescence Applications in Biotechnology and Life Sciences*; John Wiley & Sons, Inc.: Hoboken, NJ, 2009.
- Michalet, X.; Pinaud, F. F.; Bentolila, L. A.; Tsay, J. M.; Doose, S.; Li, J. J.; Sundaresan, G.; Wu, A. M.; Gambhir, S. S.; Weiss, S. Quantum Dots for Live Cells, *In Vivo* Imaging, and Diagnostics. *Science* **2005**, *307*, 538–544.
- Westbrook, C.; Roth, C.; Talbot, J. *MRI in Practice*, 4th ed.; Wiley-Blackwell: Oxford, 2011.
- Laurent, S.; Forge, D.; Port, M.; Roch, A.; Robic, C.; Vander Elst, L.; Muller, R. N. Magnetic Iron Oxide Nanoparticles: Synthesis, Stabilization, Vectorization, Physicochemical Characterizations, and Biological Applications. *Chem. Rev.* **2008**, *108*, 2064–2110.
- Wang, Y. X.; Hussain, S. M.; Krestin, G. P. Superparamagnetic Iron Oxide Contrast Agents: Physicochemical Characteristics and Applications in MR Imaging. *Eur. Radiol.* **2001**, *11*, 2319–2331.
- Geraldes, C. F. G. C.; Laurent, S. Classification and Basic Properties of Contrast Agents for Magnetic Resonance Imaging. *Contrast Media Mol. Imaging* **2009**, *4*, 1–23.
- Caravan, P.; Ellison, J. J.; McMurry, T. J.; Lauffer, R. B. Gadolinium(III) Chelates as MRI Contrast Agents: Structure, Dynamics, and Applications. *Chem. Rev.* **1999**, *99*, 2293–2352.
- Hüber, M. M.; Staubli, A. B.; Kustedjo, K.; Gray, M. H.; Shih, J.; Fraser, S. E.; Jacobs, R. E.; Meade, T. J. Fluorescently Detectable Magnetic Resonance Imaging Agents. *Bioconjugate Chem.* **1998**, *9*, 242–249.
- Zhang, X.; Jing, X.; Liu, T.; Han, G.; Li, H.; Duan, C. Dual-Functional Gadolinium-Based Copper(II) Probe for Selective Magnetic Resonance Imaging and Fluorescence Sensing. *Inorg. Chem.* **2012**, *51*, 2325–2331.

12. Kelly, K. A.; Allport, J. R.; Tsourkas, A.; Shinde-Patil, V. R.; Josephson, L.; Weissleder, R. Detection of Vascular Adhesion Molecule-1 Expression Using a Novel Multimodal Nanoparticle. *Circ. Res.* **2005**, *96*, 327–336.
13. Mulder, W. J. M.; Koole, R.; Brandwijk, R. J.; Storm, G.; Chin, P. T. K.; Strijkers, G. J.; de Mello Donegá, C.; Nicolay, K.; Griffioen, A. W. Quantum Dots with a Paramagnetic Coating as a Bimodal Molecular Imaging Probe. *Nano Lett.* **2006**, *6*, 1–6.
14. Bridot, J.-L.; Dayde, D.; Rivière, C.; Mandon, C.; Billotey, C.; Lerondel, S.; Sabattier, R.; Cartron, G.; Le Pape, A.; Blondiaux, G.; et al. Hybrid Gadolinium Oxide Nanoparticles Combining Imaging and Therapy. *J. Mater. Chem.* **2009**, *19*, 2328.
15. Shi, Z.; Neoh, K. G.; Kang, E. T.; Shuter, B.; Wang, S.-C. Bifunctional Eu³⁺-Doped Gd₂O₃ Nanoparticles as a Luminescent and T₁ Contrast Agent for Stem Cell Labeling. *Contrast Media Mol. Imaging* **2010**, *5*, 105–111.
16. Jung, J.; Kim, M. A.; Cho, J.-H.; Lee, S. J.; Yang, I.; Cho, J.; Kim, S. K.; Lee, C.; Park, J. K. Europium-Doped Gadolinium Sulfide Nanoparticles as a Dual-Mode Imaging Agent for T₁-Weighted MR and Photoluminescence Imaging. *Biomaterials* **2012**, *33*, 5865–5874.
17. Zhou, J.; Sun, Y.; Du, X.; Xiong, L.; Hu, H.; Li, F. Dual-Modality *In Vivo* Imaging Using Rare-Earth Nanocrystals with Near-Infrared to Near-Infrared (NIR-to-NIR) Upconversion Luminescence and Magnetic Resonance Properties. *Biomaterials* **2010**, *31*, 3287–3295.
18. Bouzigues, C.; Gacoin, T.; Alexandrou, A. Biological Applications of Rare-Earth Based Nanoparticles. *ACS Nano* **2011**, *5*, 8488–8505.
19. Mialon, G.; Türkcan, S.; Alexandrou, A.; Gacoin, T.; Boilot, J.-P. New Insights into Size Effects in Luminescent Oxide Nanocrystals. *J. Phys. Chem. C* **2009**, *113*, 18699–18706.
20. Casanova, D.; Bouzigues, C.; Nguyen, T.-L.; Ramodiharilafy, R. O.; Bouzahir-Sima, L.; Gacoin, T.; Boilot, J.-P.; Tharaux, P.-L.; Alexandrou, A. Single Europium-Doped Nanoparticles Measure Temporal Pattern of Reactive Oxygen Species Production inside Cells. *Nat. Nanotechnol.* **2009**, *4*, 581–585.
21. D'Autréaux, B.; Toledano, M. B. ROS as Signalling Molecules: Mechanisms That Generate Specificity in ROS Homeostasis. *Nat. Rev. Mol. Cell Biol.* **2007**, *8*, 813–824.
22. Rhee, S. G. Cell Signaling. H₂O₂, a Necessary Evil for Cell Signaling. *Science* **2006**, *312*, 1882–1883.
23. Clempus, R. E.; Griendling, K. K. Reactive Oxygen Species Signaling in Vascular Smooth Muscle Cells. *Cardiovasc. Res.* **2006**, *71*, 216–225.
24. Sundaresan, M.; Yu, Z. X.; Ferrans, V. J.; Irani, K.; Finkel, T. Requirement for Generation of H₂O₂ for Platelet-Derived Growth Factor Signal Transduction. *Science* **1995**, *270*, 296–299.
25. Hensley, K.; Robinson, K. A.; Gabbita, S. P.; Salsman, S.; Floyd, R. A. Forum on Therapeutic Applications of Reactive Oxygen and Nitrogen Species in Human Disease. *Free Radical Biol. Med.* **2000**, *28*, 1449–1450.
26. Wolfbeis, O.; Dürkop, A. A Europium Ion Based Luminescent Sensing Probe for Hydrogen Peroxide. *Angew. Chem., Int. Ed.* **2002**, *1*, 4495–4498.
27. Belousov, V. V.; Fradkov, A. F.; Lukyanov, K. A.; Staroverov, D. B.; Shakhbazov, K. S.; Terskikh, A. V.; Lukyanov, S. Genetically Encoded Fluorescent Indicator for Intracellular Hydrogen Peroxide. *Nat. Methods* **2006**, *3*, 281–286.
28. Miller, E. W.; Tulyathan, O.; Tulyanthan, O.; Isacoff, E. Y.; Chang, C. J. Molecular Imaging of Hydrogen Peroxide Produced for Cell Signaling. *Nat. Chem. Biol.* **2007**, *3*, 263–267.
29. Lee, D.; Khaja, S.; Velasquez-Castano, J. C.; Dasari, M.; Sun, C.; Petros, J.; Taylor, W.; Murthy, N. *In Vivo* Imaging of Hydrogen Peroxide with Chemiluminescent Nanoparticles. *Nat. Mater.* **2007**, *6*, 765–769.
30. Bouzigues, C. I.; Nguyen, T.-L.; Ramodiharilafy, R.; Claeson, A.; Tharaux, P.-L.; Alexandrou, A. Regulation of the ROS Response Dynamics and Organization to PDGF Motile Stimuli Revealed by Single Nanoparticle Imaging. *Chem. Biol.* **2014**, *21*, 647–656.
31. Türkcan, S.; Masson, J.-B.; Casanova, D.; Mialon, G.; Gacoin, T.; Boilot, J.-P.; Popoff, M. R.; Alexandrou, A. Observing the Confinement Potential of Bacterial Pore-Forming Toxin Receptors inside Rafts with Nonblinking Eu³⁺-Doped Oxide Nanoparticles. *Biophys. J.* **2012**, *102*, 2299–2308.
32. Türkcan, S.; Alexandrou, A.; Masson, J.-B. A Bayesian Inference Scheme To Extract Diffusivity and Potential Fields from Confined Single-Molecule Trajectories. *Biophys. J.* **2012**, *102*, 2288–2298.
33. Cuzzocrea, S.; Riley, D. P.; Caputi, A. P.; Salvemini, D. Antioxidant Therapy: A New Pharmacological Approach in Shock, Inflammation, and Ischemia/Reperfusion Injury. *Pharmacol. Rev.* **2001**, *53*, 135–159.
34. Chinta, S. J.; Andersen, J. K. Redox Imbalance in Parkinson's Disease. *Biochim. Biophys. Acta* **2008**, *1780*, 1362–1367.
35. Gupta, S. C.; Hevia, D.; Patchva, S.; Park, B.; Koh, W.; Aggarwal, B. B. Upsides and Downsides of Reactive Oxygen Species for Cancer: The Roles of Reactive Oxygen Species in Tumorigenesis, Prevention, and Therapy. *Antioxid. Redox Signal.* **2012**, *16*, 1295–1322.
36. Toyokuni, S.; Okamoto, K.; Yodoi, J.; Hiai, H. Persistent Oxidative Stress in Cancer. *FEBS Lett.* **1995**, *358*, 1–3.
37. Ishikawa, K.; Takenaga, K.; Akimoto, M.; Koshikawa, N.; Yamaguchi, A.; Imanishi, H.; Nakada, K.; Honma, Y.; Hayashi, J.-I. ROS-Generating Mitochondrial DNA Mutations Can Regulate Tumor Cell Metastasis. *Science* **2008**, *320*, 661–664.
38. Ramsey, M. R.; Sharpless, N. E. ROS as a Tumour Suppressor? *Nat. Cell Biol.* **2006**, *8*, 1213–1215.
39. Liu, B.; Chen, Y.; Clair, D. S. ROS and p53: A Versatile Partnership. *Free Radical Biol. Med.* **2008**, *44*, 1529–1535.
40. Van de Bittner, G. C.; Bertozzi, C. R.; Chang, C. J. Strategy for Dual-Analyte Luciferin Imaging: *In Vivo* Bioluminescence Detection of Hydrogen Peroxide and Caspase Activity in a Murine Model of Acute Inflammation. *J. Am. Chem. Soc.* **2013**, *135*, 1783–1795.
41. Van de Bittner, G. C.; Dubikovskaya, E. A.; Bertozzi, C. R.; Chang, C. J. *In Vivo* Imaging of Hydrogen Peroxide Production in a Murine Tumor Model with a Chemoselective Bioluminescent Reporter. *Proc. Natl. Acad. Sci. U.S.A.* **2010**, *107*, 21316–21321.
42. Lippert, A. R.; Keshari, K. R.; Kurhanewicz, J.; Chang, C. J. A Hydrogen Peroxide-Responsive Hyperpolarized ¹³C MRI Contrast Agent. *J. Am. Chem. Soc.* **2011**, *133*, 3776–3779.
43. Huignard, A.; Gacoin, T.; Boilot, J.-P. Synthesis and Luminescence Properties of Colloidal YVO₄:Eu Phosphors. *Chem. Mater.* **2000**, *12*, 1090–1094.
44. Huignard, A.; Buisette, V.; Laurent, G.; Gacoin, T.; Boilot, J.-P. Synthesis and Characterizations of YVO₄:Eu Colloids. *Chem. Mater.* **2002**, *14*, 2264–2269.
45. Jin, D.; Yang, H.; Ding, G.; Yu, X.; Wang, L.; Zheng, Y. Hydrothermal Synthesis and Photoluminescence Behavior of Eu-Doped GdVO₄. *Inorg. Mater.* **2008**, *44*, 1121–1124.
46. Zheng, F.; Wang, W.; Yang, P. GdVO₄:Ln (Ln = Eu, Dy, and Sm) Microstructures: Solvothermal and Luminescent Properties. *J. Optoelectron. Adv. Mater.* **2011**, *5*, 596–599.
47. Aslan, K.; Wu, M.; Lakowicz, J. R.; Geddes, C. D. Fluorescent Core–Shell Ag@SiO₂ Nanocomposites for Metal-Enhanced Fluorescence and Single Nanoparticle Sensing Platforms. *J. Am. Chem. Soc.* **2007**, *129*, 1524–1525.
48. Lauffer, R. B. Paramagnetic Metal Complexes as Water Proton Relaxation Agents for NMR Imaging: Theory and Design. *Chem. Rev.* **1987**, *87*, 901–927.
49. Aime, S.; Botta, M.; T. E. Gd(III)-Based Contrast Agents for MRI. *Adv. Inorg. Chem.* **2005**, *57*, 173–237.
50. Sengers, J. V.; Watson, J. T. R. Improved International Formulations for the Viscosity and Thermal Conductivity of Water Substance. *J. Phys. Chem. Ref. Data* **1986**, *15*, 1291.
51. Powell, D. H.; Dhubhghaill, O. M. N.; Pubanz, D.; Helm, L.; Lebedev, Y. S.; Schlaepfer, W.; Merbach, A. E. Structural and Dynamic Parameters Obtained from ¹⁷O NMR, EPR, and NMRD Studies of Monomeric and Dimeric Gd³⁺ Complexes of Interest in Magnetic Resonance Imaging: An Integrated and Theoretically Self-Consistent Approach 1. *J. Am. Chem. Soc.* **1996**, *118*, 9333–9346.

52. Van Vleck, J. *The Theory of Electric and Magnetic Susceptibilities*; Oxford University Press: Oxford, 1932.
53. Caillé, J. M.; Lemanceau, B.; Bonnemain, B. Gadolinium as a Contrast Agent for NMR. *Am. J. Neuroradiol.* **1983**, *4*, 1041–1042.
54. Penfield, J. G.; Reilly, R. F. What Nephrologists Need To Know about Gadolinium. *Nat. Clin. Pract. Nephrol.* **2007**, *3*, 654–668.
55. Haley, T. J.; Komesu, N.; Colvin, G.; Koste, L.; Upham, H. C. Pharmacology and Toxicology of Europium Chloride. *J. Pharm. Sci.* **1965**, *54*, 643–645.
56. Buissette, V.; Giaume, D.; Gacoin, T.; Boilot, J.-P. Aqueous Routes to Lanthanide-Doped Oxide Nanophosphors. *J. Mater. Chem.* **2006**, *16*, 529.
57. Beyersmann, D.; Hartwig, A. Carcinogenic Metal Compounds: Recent Insight into Molecular and Cellular Mechanisms. *Arch. Toxicol.* **2008**, *82*, 493–512.
58. Sanchez, D.; Ortega, A.; Domingo, J. L.; Corbella, J. Developmental Toxicity Evaluation of Orthovanadate in the Mouse. *Biol. Trace Elem. Res.* **1991**, *30*, 219–226.
59. Hifumi, H.; Yamaoka, S.; Tanimoto, A.; Citterio, D.; Suzuki, K. Gadolinium-Based Hybrid Nanoparticles as a Positive MR Contrast Agent. *J. Am. Chem. Soc.* **2006**, *128*, 15090–15091.
60. Huang, C.-C.; Liu, T.-Y.; Su, C.-H.; Lo, Y.-W.; Chen, J.-H.; Yeh, C.-S. Superparamagnetic Hollow and Paramagnetic Porous Gd₂O₃ Particles. *Chem. Mater.* **2008**, *20*, 3840–3848.
61. Port, M.; Meyer, D.; Bonnemain, B.; Corot, C.; Schaefer, M.; Rousseaux, O.; Simonot, C.; Bourrinet, P.; Benderbous, S.; Dencausse, A.; *et al.* P760 and P775: MRI Contrast Agents Characterized by New Pharmacokinetic Properties. *MAGMA* **1999**, *8*, 172–176.
62. Na, H. B.; Song, I. C.; Hyeon, T. Inorganic Nanoparticles for MRI Contrast Agents. *Adv. Mater.* **2009**, *21*, 2133–2148.
63. Corot, C.; Robert, P.; Idée, J.-M.; Port, M. Recent Advances in Iron Oxide Nanocrystal Technology for Medical Imaging. *Adv. Drug Delivery Rev.* **2006**, *58*, 1471–1504.
64. Moeller, M. J.; Tenten, V. Renal Albumin Filtration: Alternative Models to the Standard Physical Barriers. *Nat. Rev. Nephrol.* **2013**, *9*, 266–277.
65. Choi, H. S.; Liu, W.; Misra, P.; Tanaka, E.; Zimmer, J. P.; Iyengar, B.; Bawendi, M. G.; Frangioni, J. V. Renal Clearance of Quantum Dots. *Nat. Biotechnol.* **2007**, *25*, 1165–1170.
66. Dutz, S.; André, W.; Hergt, R.; Müller, R.; Oestreich, C.; Schmidt, C.; Töpfer, J.; Zeisberger, M.; Bellemann, M. E. Influence of Dextran Coating on the Magnetic Behaviour of Iron Oxide Nanoparticles. *J. Magn. Magn. Mater.* **2007**, *311*, 51–54.
67. Bass, M.; DeCusatis, C. M.; Enoch, J. M.; Lakshminarayanan, V.; Li, G.; MacDonald, C.; Mahajan, V. N.; Van Stryland, E. *Handbook of Optics. Optical Properties of Materials, Non-linear Optics, Quantum Optics*; McGraw-Hill: Columbus, OH, 2010; Vol. IV.